

1 Required sampling-density of ground-based soil moisture and brightness
2 temperature observations for calibration/validation of L-band satellite
3 observations based on a virtual reality
4

5 Shaoning Lv^{1*}, Bernd Schalge¹, Pablo Saavedra Garfias², Clemens Simmer¹

6 1. Institute for Geosciences - Section Meteorology at the University of Bonn, Auf dem Huegel 20, 53121
7 Bonn, Germany; 2. Geophysical Institute at the University of Bergen, Allégaten 70, 5020 Bergen, Norway.
8

9 **Abstract:** Microwave remote sensing is the most promising tool for monitoring near-surface soil moisture
10 distributions globally. With the Soil Moisture and Ocean Salinity (SMOS) and Soil Moisture Active Passive
11 (SMAP) missions in orbit, considerable efforts are made to evaluate derived soil moisture products via
12 ground observations, microwave transfer simulation, and independent remote sensing retrievals. Due to
13 the large footprint of the satellite radiometers of about 40 km in diameter and the spatial heterogeneity
14 of soil moisture, minimum sampling densities for soil moisture are required to challenge the targeted
15 precision. Here we use 400 m resolution simulations with the regional Terrestrial System Modeling
16 Platform (TerrSysMP) and its coupling with the Community Microwave Emission Modelling platform
17 (CMEM) to quantify the maximum sampling distance allowed for soil moisture and brightness
18 temperature validation. Our analysis suggests that an overall sampling distance of finer than 6 km is
19 required to validate the targeted accuracy of $0.04 \text{ cm}^3/\text{cm}^3$ with a 70% confidence level in SMOS and SMAP
20 estimates over typical mid-latitude European regions. The maximum allowed sampling distance depends
21 on the land-surface heterogeneity and the meteorological situation, which influences the soil moisture
22 patterns, and ranges from about 6 km to 17 km for a 70% confidence level for a typical year. At the
23 maximum allowed sampling distance on a 70% confidence level, the accuracy of footprint-averaged soil
24 moisture is equal or better than brightness temperature estimates over the same area. Estimates strongly
25 deteriorate with larger sampling distances. For the evaluation of the smaller footprints of the active and
26 active/passive products of SMAP the required sampling densities increase; e.g., when a grid resolution of
27 3 km diameter is sampled by 3 sites of footprints of 9 km sampled by 5 sites required already only 50%-
28 60% of the pixels have a sampling error below the nominal values. The required minimum sampling
29 densities for ground-based radiometer networks to estimate footprint averaged brightness temperature
30 are higher than for soil moisture due to the non-linearities of radiative transfer, and only weakly
31 correlated in space and time. This study provides a basis for a better understanding of the sometimes
32 strong mismatches between derived satellite soil moisture products and ground-based measurements.

33 **Key words:** passive microwaves, soil moisture, brightness temperature, sampling density

34 **1. Introduction**

35 Information on the global soil moisture distribution is required, e.g., for weather forecasting, climate
36 research, and agricultural applications. Due to the high spatial variability of soil moisture, its in-situ
37 observation is practically impossible on continental scales. Passive microwave satellite remote sensing at
38 L-band frequencies may achieve this goal because of the strong dependency of the soil dielectric constant
39 on soil moisture, the - compared to higher frequencies - reduced sensitivity of the brightness
40 temperatures to surface roughness and vegetation (Njoku and Kong, 1977;Ulaby et al., 1986), and the
41 high transparency of the atmosphere at these wavelengths. The first operational L-band soil moisture
42 detection satellite, SMOS (Soil Moisture and Ocean Salinity) was launched in 2008 (Kerr et al., 2010) and
43 was followed in 2015 by SMAP (Soil Moisture Active Passive), which initially were performing with an
44 active instrument to achieve higher spatial resolution (Entekhabi et al., 2010); the active component did
45 fail, however, shortly after the full operation of the satellite. Both satellites are currently continuously and
46 globally observing passive microwave brightness temperatures, from which soil moisture products are
47 derived at a spatial resolution of 36 km and 9 km.

48 Before and after the launch of SMOS and SMAP several soil moisture monitoring networks for
49 evaluation and retrieval algorithm development were established, such as ESA's efforts at the Valencia
50 Anchor Station (VAS) in eastern Spain, SMOSREX (Surface Monitoring Of Soil Reservoir Experiment) in
51 France, the upper Danube watershed located in southern Germany (Delwart et al., 2008;de Rosnay et al.,
52 2006;dall'Amico et al., 2012;Kerr et al., 2016), and the SMAP Cal/Val project (Colliander et al.,
53 2017a;Burgin et al., 2017;Chen et al., 2017;Chen et al., 2018). All those networks have been established
54 since ground truth should be the only standard to evaluate these products. According to the Level 1
55 baseline and the minimum SMAP science requirements (SMAP Science Data Cal/Val Plan, O'Neill et al.,
56 2015) the spatial resolution of Level 2 (Passive Soil Moisture Product L2_SM_P) and Level 3 (daily
57 composite L3_SM_P) soil moisture products is 36 km, which have to reach an accuracy for soil moisture
58 of $0.04 \text{ cm}^3/\text{cm}^3$ with a probability of 70%. A wide range of measurement techniques and protocols exist
59 for setting up and performing ground-based observations for such evaluations. SMAP Cal/Val suggests
60 that volumetric soil moisture should be observed in-situ at 5 cm and 100 cm depth; optimal
61 sensing/mounting depths are, however, still debated (Lv et al., 2016a; Lv et al., 2018; Lv et al., 2019). For
62 core validation sites a minimum of six stations should cover one SMAP grid cell or footprint (O'Neill et al.,
63 2015; Famiglietti et al., 2008); but this value has not yet been shown to guarantee the nominal accuracy
64 by a thorough analysis (Jackson et al., 2012; Crow et al., 2012). More recent results show that the spatial
65 representativeness of the soil moisture tends to increase with the timescale of data series, but so does
66 their spread (Molero et al., 2018). For Cal/Val, it is required to have instantaneous soil moisture values
67 rather than averages in different timescales. Relevant studies typically use ground-based soil moisture
68 networks with fixed average sampling distance over rather homogeneous land surfaces, which are,
69 however, not necessarily representative for all land surface types. For SMAP core calibration/validation
70 sites, the data product grid-cell should be sampled with at least eight stations to reach with 70%

71 confidence an estimated soil moisture uncertainty of $0.03 \text{ m}^3/\text{m}^3$ given a spatial soil moisture standard
72 deviation of $0.07 \text{ m}^3/\text{m}^3$ as assessed from field measurements (Colliander et al., 2017b). According to the
73 same source, grid-cells with a dimension of 9 km (as for downscaled SMAP products) should be sampled
74 with at least five stations and pixels with 3 km diameter with at least three stations to reach with 70 %
75 confidence an accuracy of 0.03 and $0.05 \text{ m}^3/\text{m}^3$, respectively, while assuming a spatial soil moisture
76 standard deviation of $0.05 \text{ m}^3/\text{m}^3$ within the grid-cell.

77 Ochsner et al., (2013) point out that too few resources are currently devoted to in-situ soil moisture
78 monitoring networks, and that despite their increasing number, a standard for network density and
79 sampling procedures are missing. The International Soil Moisture Network (ISMN,
80 <https://ismn.geo.tuwien.ac.at/en/>) is an effort for unifying global soil moisture observation networks
81 (Dorigo et al., 2011). Coopersmith et al., (2016) suggested temporary network extensions around
82 permanent installations to quantify the representativeness of the latter. Qin et al., (2013) suggested the
83 use of MODIS-derived apparent thermal inertia to interpolate between in-situ soil moisture
84 measurements. So far, the required sampling density is discussed only concerning in-situ measurements,
85 which heavily depend on sensor quality and network location (Vereecken et al., 2008; Brocca et al., 2010;
86 Bhuiyan et al., 2018). Higher station numbers are necessary, as well as the establishment of general rules
87 for their selection (Cosh et al., 2017). Chen et al. (2017, 2018, 2019) suggest the utilization of TC (Triple
88 collocation), which is a statistic method to characterize systematic biases and random errors, or ETC
89 (Extended Triple collocation) to analyze the noise component in soil moisture observations, and to use
90 correlation to evaluate the representativeness of soil moisture networks. They also suggest that the core
91 validation sites should allow validating the retrieved soil moisture to an accuracy of $0.04 \text{ cm}^3/\text{cm}^3$ with a
92 probability of 70% in terms of unbiased RMSE because the bias itself is hard to eliminate.

93 Establishing ground monitoring networks for calibration/validation of soil moisture products from
94 satellite L-band observations is challenging partly due to the different spatial scales between observations
95 from soil moisture sensors and satellites. Moreover, from a direct comparison between satellite soil
96 moisture products and ground-based measurements from existing soil moisture networks, it is impossible
97 to isolate the sampling error, and only very few studies investigate systematically the station density
98 required to allow for a given accuracy taking the land heterogeneity into account. In our study, we use a
99 400-m resolution virtual reality generated with a regional terrestrial modeling system coupled with an
100 observation operator to estimate such minimum station densities. The virtual reality contains realistic soil,
101 land cover, and topography variability and allows us to arbitrarily vary the sampling density and, thus,
102 average sampling distance in steps of 400 m. Section 2 introduces the virtual reality, and the observation
103 operator used to transfer the terrestrial system states into virtual observations. In Section 3, we derive
104 the error growth with increasing average sampling distance for soil moisture and brightness temperatures.
105 Conclusions and discussion are provided in Section 4.

106 **2. Methodology and data**

107 **2.1 Virtual reality**

108 The modeling system used to create the virtual reality from which we draw the virtual soil moisture
 109 observations and compute brightness temperatures is the Terrestrial Systems Modeling Platform
 110 (TerrSysMP, Shrestha et al., 2014; Gasper et al., 2014; Sulis et al., 2015) developed within the framework
 111 of the Transregional Collaborative Research Center 32 (TR32, Simmer et al., 2015). TerrSysMP consists of
 112 the atmospheric model COSMO (Consortium For Small Scale Modelling, Baldauf et al., 2011), the land
 113 surface model CLM (Community Land Model Version 3.5, Oleson et al., 2008), and the distributed
 114 hydrological model ParFlow v693 (Ashby and Falgout, 1996;Kollet et al., 2010). The platform, specially
 115 designed for high-performance computing environments (Gasper et al., 2014), has been extensively
 116 evaluated against observations (Sulis et al., 2015, 2018; Shrestha et al., 2018b) as well as similar regional
 117 terrestrial system models (Sulis et al., 2017). The effect of spatial resolution on simulated soil moisture
 118 and the resulting exchange fluxes between land and atmosphere has been studied with TerrSysMP by
 119 Shrestha et al. (2015, 2018a).

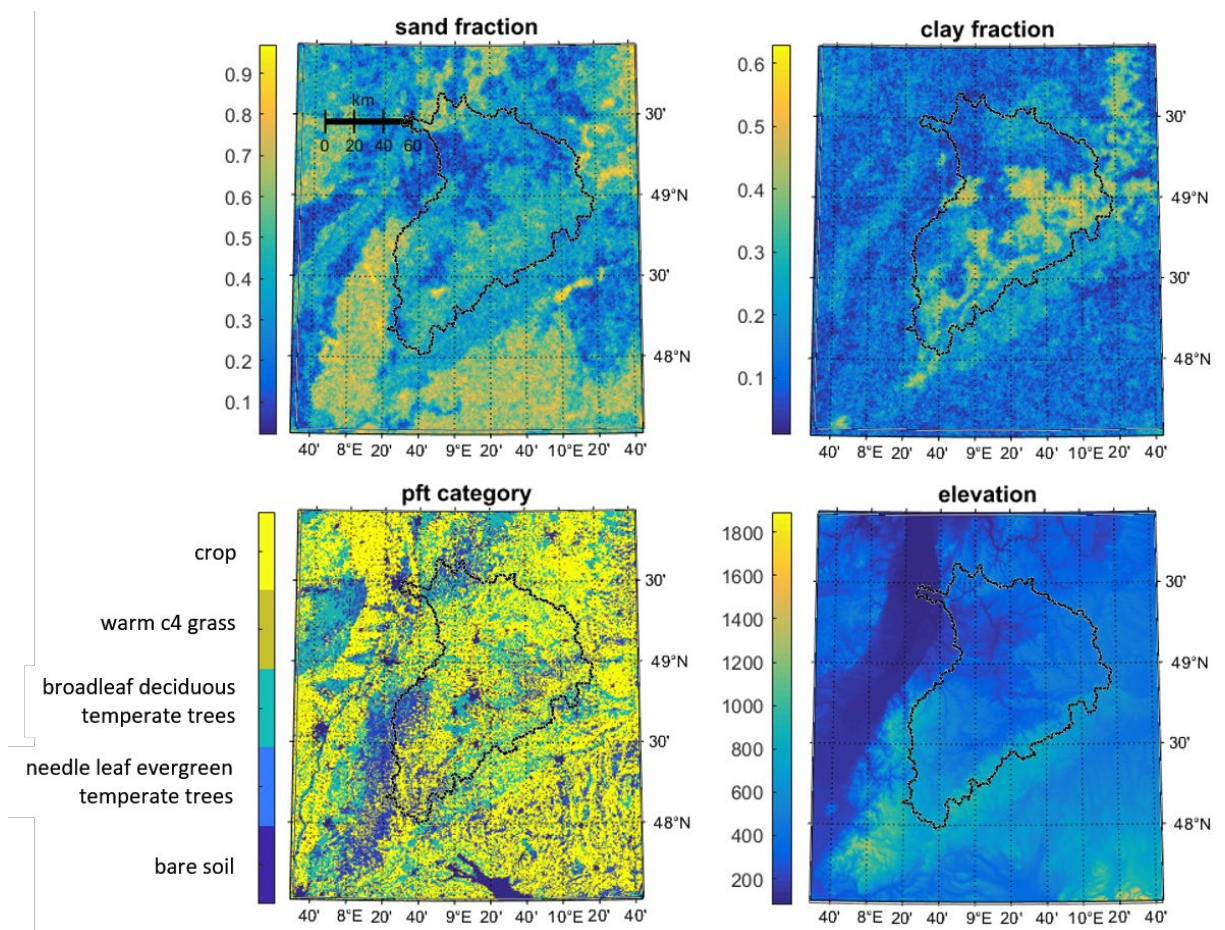


Figure 1: TerrSysMP simulation area at 400 m resolution with the Neckar catchment roughly in the center indicated by the black line. Soil sand (left) and clay fractions (right) are displayed in the upper row sub-figures, while the Plant Functional Types (PTFs) used by CLM are shown in the lower left sub-figure, and topography (in m) in the lower right sub-figure.

121 We use for this study available simulation results generated by the research unit FOR2131 (Schalge
122 et al., 2019; Schalge et al., 2016) over an area containing the Neckar catchment in southwestern Germany
123 in its center (Figure 1). CLM and ParFlow were run at the horizontal computational grid with 400 m
124 resolution. ParFlow has 50 vertical soil layers in which the upper ten coincide with the ten soil layers of
125 CLM. The vertical resolution is variable with smaller steps near the land surface. The atmospheric model
126 COSMO runs at a 1.1 km horizontal resolution, and COSMO is forced at the lateral boundaries with a
127 COSMO-DE analysis from the operational weather forecast run by the German national weather service
128 (Deutscher Wetterdienst, DWD) available at hourly time steps. The main topographic features of the
129 modeling area are the upper Rhine valley in the west, the Black Forest in the southwest, and the foothills
130 of the Alps in the south. The heights range from 80 m to 1900 m. The area was selected by the research
131 unit because of its heterogeneity in topography and land-use typical for midlatitude European river
132 catchments; thus, it is also well suited for our study. The objective of the research unit is the setup and
133 test of a strongly coupled data assimilation system with a fully-coupled regional terrestrial model. Their
134 virtual reality run (VR01), the results of which we are exploiting in this study, is the so-called nature run
135 from which the research unit draws the virtual observations to be assimilated in a lower-resolved model
136 version using ensemble methods. The model area can be covered by about 15 x 20 SMOS pixels, which
137 suffices for the statistical analyses performed to determine required sampling densities. There exist two
138 soil moisture monitoring networks close to the domain, which are used for soil moisture validation studies
139 with satellite-based L-band observations (Montzka et al., 2013).

140 The topographic data for VR01 is obtained from the European Environment Agency EEA
141 (<http://www.eea.europa.eu/data-and-maps/data/eu-dem>), which is also the source for the CORINE land
142 use data (<http://www.eea.europa.eu/data-and-maps/data/corine-land-cover-2006-raster-3>) used to
143 characterize vegetation in the model domain. Since CORINE uses many more land-use classes than CLM,
144 the CORINE classes are aggregated to the five classes discriminated in the CLM in the modeling area:
145 broadleaf forests which can be found mostly in hilly areas throughout the domain in smaller patches,
146 needle leaf forests which dominate at higher elevation such as the Black Forest, grassland which is
147 relatively rare and only appears in small patches, and crops which is the most dominant land use type
148 throughout the domain and appears almost anywhere. All other classes, such as urban areas, are treated
149 as bare soil in VR01.

150 The Leaf Area Index (LAI) for the specific plant classes is taken from MODIS estimates corrected for
151 known biases (Tian et al., 2004). Instead of the tiling approach implemented in CLM, the dominant land
152 use type for each grid-cell is used, because the resolution of 400 m is high enough to warrant this approach.
153 The SAI (Stem Area Index) is estimated from the LAI by formulations slightly modified from those
154 implemented in the CLM. For crops, SAI is just 10% of the LAI; thus, SAI is larger in summer than in winter.
155 For all other types, SAI is 10% of LAI plus a "dead leaf" component. The "dead leaf" component is
156 estimated empirically from the change of the LAI from the previous and current month. The "dead leaf"
157 component is only a major contributor during fall, but even there the needle leaf trees, for instance, show

158 only a small increase of SAI. The VR01 region is mostly covered by deciduous trees that have 1-2 months
159 of high SAI because the dead-leaf component decays rather quickly. Details about SAI calculation in VR01
160 are described in Schalge et al., (2016), Lawrence and Chase, (2007), and Zeng et al., (2002).

161 The soil map (Figure 1, upper row) is derived from a product of the German Federal Institute for
162 Geosciences and Natural Resources BGR ([http://www.bgr.bund.de/DE/Themen/Boden/
163 Informationsgrundlagen/Bodenkundliche_Karten_Datenbanken/BUEK1000/buek1000_node.html](http://www.bgr.bund.de/DE/Themen/Boden/Informationsgrundlagen/Bodenkundliche_Karten_Datenbanken/BUEK1000/buek1000_node.html)). Soil
164 values for regions near the edge of the modeling domain in France and Switzerland are extrapolated.
165 Variability was added to the relatively large polygons of constant soil parameters to represent better what
166 would be found in reality at higher resolutions following (Baroni et al., 2017). The soil color is derived from
167 the carbon content of the soil with carbon-rich soils being darker, except for the bare soil areas, which all
168 use the same relatively light color class. There is deep soil geology included in ParFlow as well as alluvial
169 channels below rivers to account for deeper subsurface flow, but these features will not directly impact
170 the results shown here as they only appear below the soil layers.

171 **2.2 Generation of L-Band passive microwave observations**

172 The radiative transfer model CMEM (Rosnay et al., 2009) computes the land emissivity based on a
173 dielectric mixture model for soil moisture, soil sand and clay fractions, soil surface roughness, vegetation
174 optical thickness, single scattering albedo, and land surface orientation relative to the satellite viewing
175 perspective. Depending on the sand and clay fractions, brightness temperatures may vary by tens of
176 Kelvins given the same near-surface soil moisture. Vegetation optical thickness depends on LAI, which
177 varies in the VR01 with time depending on PFT type. Depending on the particular Plant Functional Type
178 (PFT), CMEM uses different parameters to calculate the vegetation optical thickness from the respective
179 LAI. Soil effective temperature is computed with a new scheme introduced by (Lv et al., 2014). The new
180 scheme is a discretization of the integral formulation and takes advantage of multi-layer soil
181 temperature/moisture profile information with a wider range of soil properties. This allows to better
182 adapt CMEM to the available land surface model data. Also, soil temperature and snow depth impact the
183 simulated brightness temperatures. More details can be found in the SMOS global surface emission model
184 handbook (Rosnay et al., 2009).

185 From the 400 m resolution brightness temperatures, virtual satellite observations are generated
186 with CMEM taking the satellite antenna function into account. Figure 2 shows the centers of the about
187 320 footprints corresponding to the SMOS L1 TB data product at 41° incidence angle for a potential
188 satellite overpass and - on the same scale - the satellite antenna function for one footprint, which changes
189 shape depending on the elevation of the individual 400 m model grid areas, orbit altitude and declination,
190 and satellite scanning and incidence angle.

191 Not each SMOS overflight will cover the whole area in reality. But in our study, we assume for
192 simplicity that all footprints indicated in Figure 2 are observed once a day at 6 a.m. local time, which
193 corresponds to the approximate ascending and descending overpass time of SMOS and SMAP,

194 respectively. The satellite footprint is much larger than the nominal satellite spatial resolution of 40 km
195 that is defined by 3 dB contour of the main lobe; thus areas much larger in diameter contribute to one
196 satellite-observed brightness temperature (i.e., 50% of one satellite-observed brightness temperature
197 originates from an area roughly ten times larger than the nominal satellite footprint).

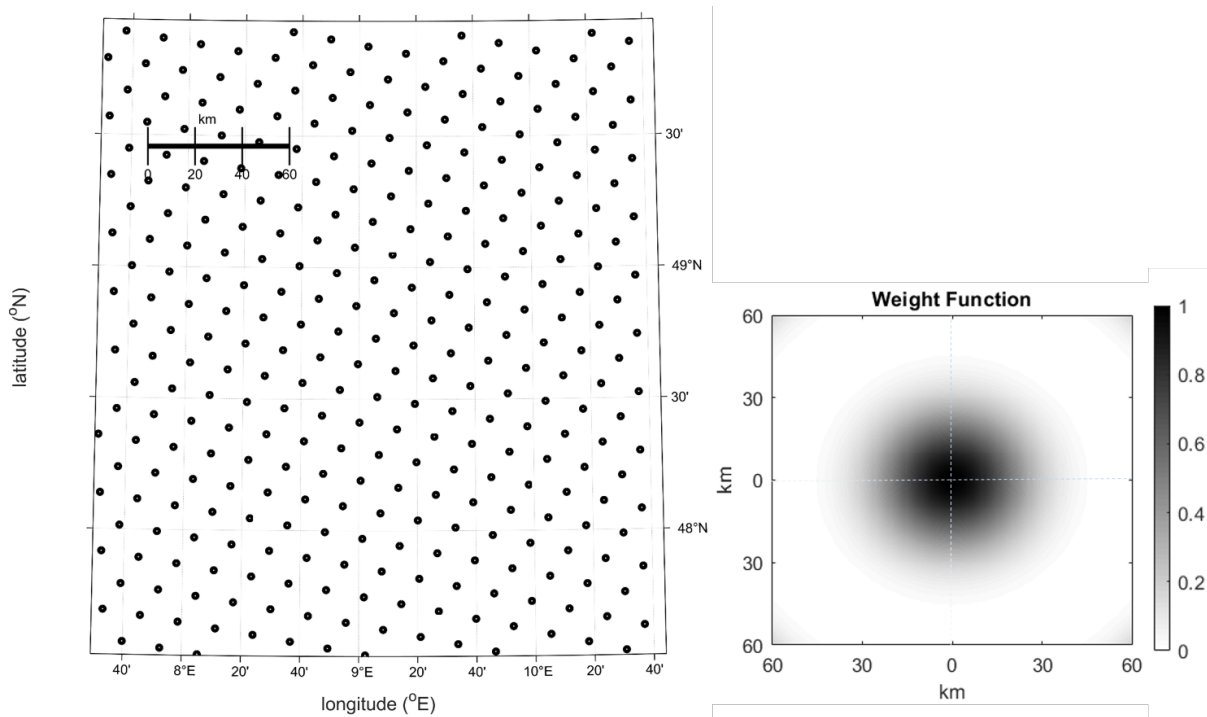


Figure 2: Dots in the left sub-figure indicate the centers of SMOS footprints for one hypothetical satellite overpass. The right sub-figure shows the antenna pattern of one satellite footprint at nadir on the same scale as the map on the left sub-figure.

198

199 The virtual reality employed in this study is a physically consistent state of the terrestrial system in
200 space and time because it has been produced by a numerical model based on the conservations equations
201 for mass, energy, and momentum. When applying the satellite observation operator to this model state,
202 we assume that the model state is correct, as well as the simulated brightness temperature. Thus, our
203 study only quantifies the impact of the sampling density of a surface network on the comparison between
204 area-averaged values and their estimates from the surface network, i.e., we ignore errors of the dynamic
205 model (TerrSysMP) and of the forward operator (CMEM). Based on the modeling results, we analyze a
206 range of ground-based network configurations with sampling points at least 400 m apart, and we assume
207 that all quantities (state of the terrestrial system and brightness temperature) do not vary within 400 m.
208 While this is an approximation, we believe that our results and their outcome can be generalized. We will
209 come back to this point in the discussion section.

210 Since one SMOS/SMAP footprint covers approximately 106x106 model grid columns in the VR01,
 211 the respective area can be sampled by one up to a maximum of 106x106 (virtual) sites. If the footprint
 212 area is sampled with n sites, there are $C_{106 \times 106}^n$ sampling combinations (SC, hereafter) possible, with

$$213 \quad SC = C_{106 \times 106}^n = \frac{106^2!}{n!(106^2 - n)!} \quad (1)$$

214 which is an unordered, non-overlapping collection of distinct elements of a prescribed size taken from a
 215 given set. For example, with a 10 km distance between sampling sites, about 6x6 sampling sites are
 216 possible within one footprint, which can be spatially distributed in $C_{106 \times 106}^{6 \times 6} \approx 1.69 \times 10^{104}$ ways. It is
 217 computationally not feasible to consider all those combinations. When, however, we first divide each
 218 footprint into equally-sized sub-areas each containing exactly one sampling site (this assumes a certain
 219 degree of homogeneity within the network (which would in reality also be strived for), the number of
 220 potential sampling networks is drastically reduced. If we set the sampling distance within a 43 x 43 km²

221 area to i km, we divide the footprint into $\left(\frac{43}{i}\right)^2$ sub-areas each containing $106 \times 106 / \left(\frac{43}{i}\right)^2 \approx 6.08 \times i^2$

222 400m-resolution model columns. When we further select within each of the equally-sized sub-areas of a
 223 satellite footprint the same model column (i.e., the one with row number k and column number l both,
 224 e.g., starting at 1 in the upper left column of each subarea), a regular equidistant observation network
 225 within the SMOS/SMAP footprints is enforced similar to the one used in the study by (Famiglietti et al.,
 226 2008). For each footprint (subscript f) at a particular time (subscript t) of a certain sampling distance (i km,
 227 subscript d), the number of network configurations SC_{ftd} is

$$228 \quad SC_{ftd} = 106 \times 106 / \left(\frac{43}{i}\right)^2 \approx \left(\frac{i}{0.406}\right)^2 \quad (2)$$

229 This results for a certain sampling distance (i km) for all 320 footprints and all 365 days of a year to a
 230 sample size of

$$231 \quad SC_{ft} = \left[106 \times 106 / \left(\frac{43}{i}\right)^2 \right] \times 365 \times 320 \quad (3)$$

232 from which we will compute the PDF of the resulting sampling errors. For each day given one observation
 233 per day for all 320 footprints and summed over all sampling distances, we get samples of size

$$234 \quad SC_{td} = \sum_{i=0.8}^{18} \left[106 \times 106 / \left(\frac{43}{i}\right)^2 \right] \times 320, \quad (4)$$

235 from which we will compute PDFs of the maximum allowed sampling distances. For each grid-cell with
 236 one observation per day taken over one year and summed over all sampling distances, we get

237
$$SC_{fd} = \sum_{i=0.8}^{18} \left[106 \times 106 / \left(\frac{43}{i} \right)^2 \right] \times 365 \quad (5)$$

238 samples, from which we determine the spatial distribution of the maximum allowed sampling distances.
 239 E.g., for 800 m sampling distance, we determine the maximum from $\left(\frac{0.8}{0.4} \right)^2 \times 365 \times 320 = 467200$
 240 samples, the number of which increases with the square of the sampling distance.

241 The sampling described above is applied to soil moisture (brightness temperature) with (without)
 242 considering the satellite weighting function (Figure 2b). Since SMAP Cal/Val requires that the nominal
 243 accuracy of 0.04 cm³/cm³ for retrievals should be met with a probability of 70%, we take the error at the
 244 70th percentile, if not specified otherwise. In the following, we mostly use the more intuitive sampling
 245 distance (km), but also the sampling density (sites per km²) when we are qualifying tendencies. The
 246 relationship between the sampling distance and the sampling density is simply

247
$$\text{sampling density} = \frac{1}{\text{sampling distance}^2} \quad (6)$$

248 E.g., the 15/5/3 sites for grid-cells with diameters of 36/9/3 km recommended by SMAP Cal/Val would be
 249 around 0.0116/0.0617/0.3333 sites per km² and correspond to a sampling distance of 9.295/4.025/1.732
 250 km. We note here that the grid size of the SMAP passive soil moisture product is 36 km x 36 km per pixel,
 251 which is the ISEA-4H9 discrete global grid for SMOS (43 km x 43 km). The 43 km in all equations shall be
 252 exchanged by 36 km when computing the number of sampling networks by equations (1) to (3).

253 **3. Results**

254 We first discuss in detail the results for soil moisture sampling. Then we extend the same methodology to
 255 brightness temperature and compare both results. We also evaluate the potential sampling error for
 256 “footprints” with grid sizes of 3 km and 9 km, because the SMAP products also include combined active-
 257 passive soil moisture retrievals at higher spatial resolutions (e.g., EASE-grid 9 km) and a product only based
 258 on the active sensor (EASE-grid 3 km). Two kinds of percentages are used in this study. One is the
 259 confidence level, which is related to the number of potential network configurations for one footprint as
 260 given by Equation (2). The other percentage is related to the PDF of the maximum allowed sampling
 261 distance with a confidence level of 70% (we also use 100% for comparison), which is based on Equation
 262 (3)/(4)/(5). The site numbers defined by SMAP are equivalent to the latter.

263 **3.1 Soil moisture**

264 We compare the true (but virtual) spatial arithmetic average of soil moisture at the SMOS/SMAP
 265 resolution with the arithmetic average of soil moisture at 0.05 m depth computed from the sampling
 266 points taken at distances ranging from 400 m (i.e., each VR01 grid column, no sampling error) to 18 km
 267 (about half the radius of a SMAP or SMOS pixel. First, we analyze the probability density function of the

268 sampling error as it varies with the sampling distance, taking the SC_{ft} samples for one whole year of all
269 footprints in the whole model area into account (Equation (3), Figures 3 and 6). Then we analyze the
270 evolution over the year of the daily PDF of the maximum allowed sampling distance (for keeping the
271 sampling error below the nominal value of $0.04 \text{ cm}^3/\text{cm}^3$ with 70% confidence) from SC_{td} samples
272 (Equation (4), Figures 4 and 7). Finally, we look at the spatial variability of the maximum allowed sampling
273 distance (for keeping the sampling error below the nominal value of $0.04 \text{ cm}^3/\text{cm}^3$ with 70% confidence)
274 based on all samples of one SMOS/SMAP pixel over the year SC_{fd} (Equation (5), Figures 5 and 8). When we
275 analyze the sampling errors for brightness temperatures, we use footprint averages weighted by the
276 antenna function; using the weighting function according to the dB pattern for soil moisture leads to
277 differences below $0.01 \text{ cm}^3/\text{cm}^3$; thus, the averaging procedure does not impact our conclusions for soil
278 moisture.

279 We compute the maximum sampling error for each sampling distance and each footprint from the
280 daily observations over one year of all network configurations. The distributions of the corresponding 320
281 values are displayed in the box-whisker plots in Figure 3 (top). Thus each value entering the distribution
282 at a given sampling distance (individual box-whisker plot in Figure 3) stems from that sampling network
283 for one of the 320 SMOS footprints, which leads to the largest sampling error taking all daily observations
284 over a year into account (Equation (3)). With a sampling distance of 400m, we exactly reproduce the true
285 (but virtual) arithmetic soil moisture average, i.e., the maximum error is zero. Maximum errors naturally
286 increase with sampling distance, as demonstrated by the widening of the maximum error distribution.
287 The median of the maximum sampling error increases almost linearly, with about $0.022 \text{ cm}^3/\text{cm}^3$ per
288 kilometer increase in sampling distance. The spread of the maximum error increases from less than 0.01
289 cm^3/cm^3 at 0.8 km to approximately $0.4 \text{ cm}^3/\text{cm}^3$ at 18 km, with quite some variability between the
290 sampling steps. To guarantee a sampling error below $0.04 \text{ cm}^3/\text{cm}^3$ (the assumed accuracy of SMOS/SMAP
291 retrievals) with 100% confidence everywhere in the region at any time of the year (Figure 3, top), the
292 maximum sampling distance should not exceed 2.8 km. With a 4.8 km sampling distance, for 50% of the
293 area and/or days of the year, we get sampling errors above $0.04 \text{ cm}^3/\text{cm}^3$. At a sampling distance of 4.4
294 km (about 18 sites within a 43 km x 43 km pixel), the same would hold for only 25% of the satellite pixels.

295 Figure 3 (bottom) displays the PDF of the maximum sampling error corresponding to the 70th
296 percentile of the sampling error PDF computed for each satellite pixel over the year. Thus, to guarantee a
297 sampling error below $0.04 \text{ cm}^3/\text{cm}^3$ for all network configurations for only up to 70% of all pixels and all
298 days of the year, a minimum sampling distance of 6 km is required. At a sampling distance of 12 km,
299 already only 50% of the pixels fulfill this requirement. Overall, about one-quarter of the stations required
300 for 100% confidence is needed, when the requirement to stay within the $0.04 \text{ cm}^3/\text{cm}^3$ error margin is
301 relaxed to 70%.

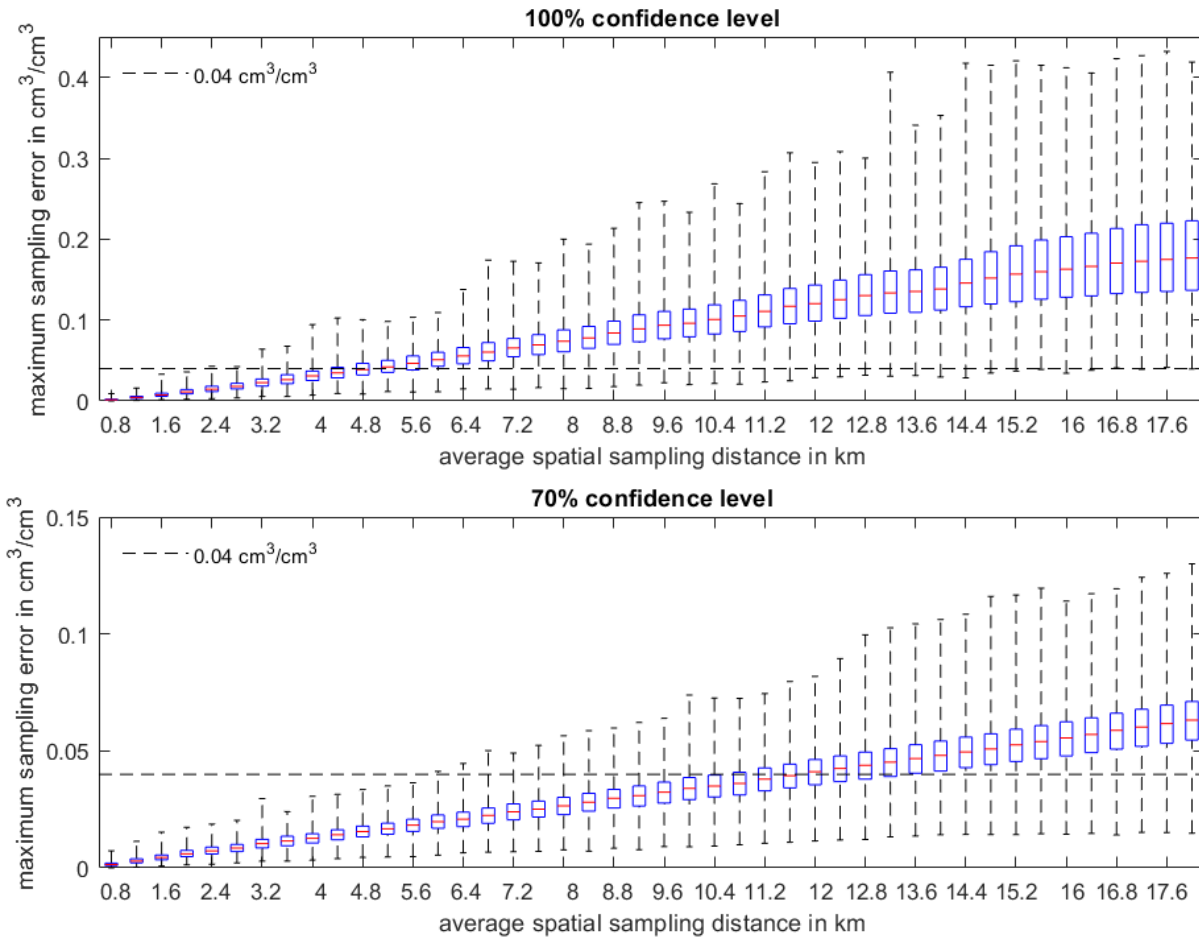


Figure 3: Box-whisker-plots (median in red, 25th- and 75th-percentiles as bounds of the box, whiskers encompass all values of the maximum sampling errors for the 320 satellite footprints of the arithmetic mean soil moisture estimated for all network configurations observing twice-a-day over one year at the given sampling distances (abscissa). The top subfigure shows the absolute maximum error, while the bottom subfigure displays the results for the 70th percentile of the sampling error distribution at each satellite footprint. The horizontal dashed line is the 0.04 cm³/cm³ retrieval error anticipated for SMOS and SMAP.

302

303

304

305

306

307

308

309

310

311

As outlined above, we can also quantify from the simulations the allowed maximum sampling distance on a daily basis from the samples with the size given by Equation (4). According to Figure 4 (bottom), for 80 % of the SMOS/SMAP pixels, the maximum allowed sampling distance is between 8.4 km and 16 km, which is 7 - 26 stations for SMOS (43 km) and 5 - 18 stations for SMAP passive (36 km) to keep the sampling error below 0.04 cm³/cm³ with 70% confidence. A seasonal variation is not obvious, but rainfall events (Figure 4, top) affect the distributions by increasing the maximum allowed sampling distances because the surface soil moisture becomes more homogeneously distributed in space due to the typically quite widespread precipitation in that region. The opposite occurs during dry periods because evaporation, draining, and runoff over various soil and land cover types tend to create spatially

312 heterogeneous soil moisture distributions, which typically reaches its maximum at intermediate soil
 313 moisture levels (Brocca et al., 2010).

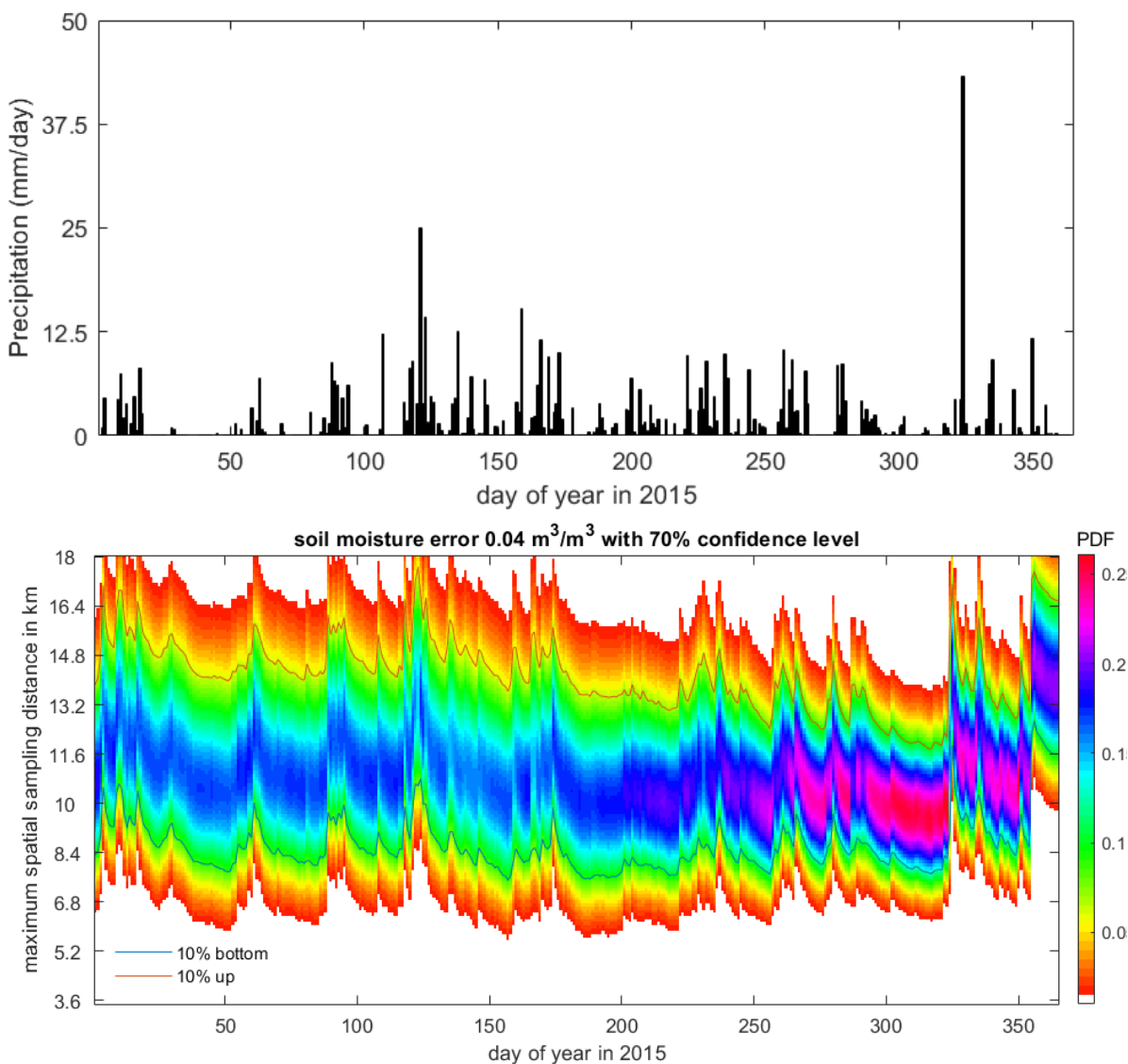


Figure 4: Precipitation in VR01 (upper panel), and time series of the distribution of the maximum allowed soil moisture sampling distance for each SMOS/SMAP pixel to assure a sampling error below 0.04 cm³/cm³ (70% confidence) for the year 2015 (bottom panel). The colored intensity is proportional to the probability of occurrence. The 10th and 90th-percentiles are indicated as blue and red lines, respectively. Every precipitation event makes soil moisture field more homogenous regarding high PDF and larger maximum spatial sampling distance, which means fewer stations required.

314
 315 The spatial distribution of the annual maximum sampling distance allowed to guarantee a sampling
 316 error below 0.04 cm³/cm³ with 70% confidence computed from the samples given by Equation (5) and its
 317 RMS for the year 2015 (Figure 5) indicates that the southeastern region requires sampling distances of

318 only below 16 km; thus only nine sites are required within a SMOS/SMAP pixel to estimate the footprint-
319 averaged soil moisture with a sampling error below $0.04 \text{ cm}^3/\text{cm}^3$. Also, the annual variation is particularly
320 small (blue). For the rest of the region, maximum allowed sampling distances range from 7 km to 10 km
321 (radius); thus, more than nine sites are required within one footprint. The annual variation of the
322 maximum sampling distances for those footprints is larger than in the southeast. The mean allowed
323 sampling distances and their day-to-day variations are only weakly correlated (correlation coefficient
324 0.40), but show larger-scale common patterns.

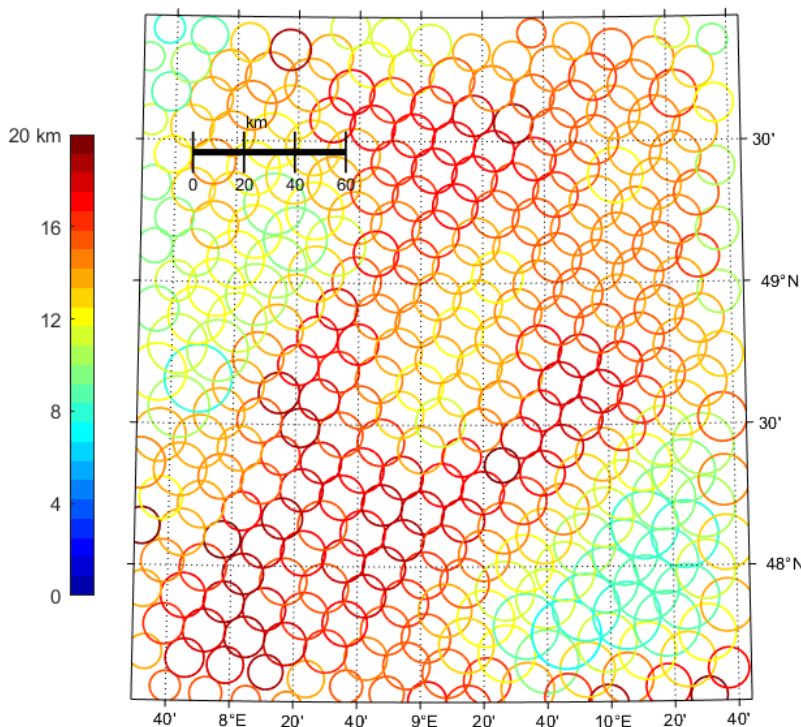


Figure 5: Spatial distribution of the mean of the maximum allowed soil moisture sampling distance in the model area required for keeping the maximum sampling error below $0.04 \text{ m}^3/\text{m}^3$ over the whole year. The circle radius indicates the maximum allowed sampling distance in the scale shown in the map, while its color (see color bar) gives the RMS of the maximum allowed sampling distance over time for the year 2015.

325

326 3.2 Brightness temperature

327 We now determine the maximum sampling distances for networks of ground-based microwave
328 radiometer allowed to estimate SMOS/SMAP footprint brightness temperatures. To this goal, we
329 transform the target accuracy of SMOS/SMAP soil moisture retrievals of $0.04 \text{ cm}^3/\text{cm}^3$ to the accuracy of
330 the corresponding brightness temperature, which is approximately 10 K for H polarization and 5 K for V
331 polarization according to CMEM forward simulations (Sabater et al., 2011; Monerris Belda, 2009). We
332 note that this brightness temperature accuracy is not the instrument observing error of the (virtual)
333 microwave radiometer, but the sensitivity of the microwave forward transfer model to soil moisture. We

334 are aware, that the radiometric accuracies of ground-based and satellite-borne sensors are much better,
 335 and that the accuracy of the soil moisture-brightness temperature relation is mainly responsible for the
 336 retrieval accuracy; thus, we use the 10K/5K uncertainty only as a proxy for the overall error.

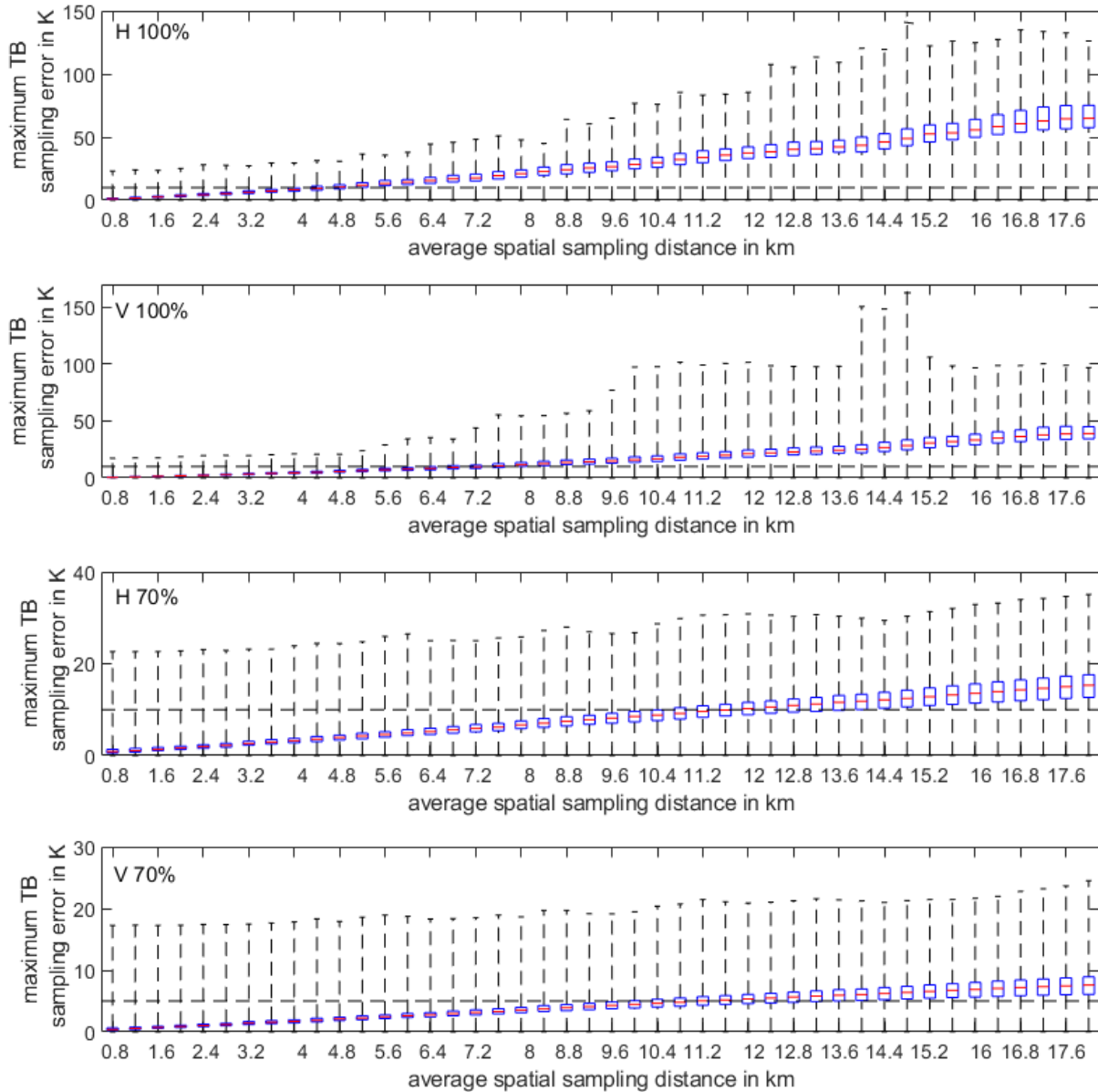


Figure 6: Same as Figure 3 but for the sampling error of the brightness temperature. The respective brightness temperature errors equivalent to a soil moisture accuracy of $0.04 \text{ cm}^3/\text{cm}^3$ of 10 K for H polarization and 5 K for V polarization are indicated as dashed horizontal lines.

337

338 By comparing the high-res TB for certain sampling distances with the antenna pattern TB from the
 339 satellite operator (Pablo & Clemens, 2017), Figure 6 shows different patterns to the soil moisture. Even at
 340 a sampling distance of 800 m, the sampling error might exceed the 10K (5K) limit in certain regions and

341 times. If we want to keep the limit with a probability of only 75 percentiles (the upper boundary of the
 342 boxes in Figure 6, 100% confidence panels), the maximum sampling distance must stay below 4.4 km. For
 343 a sampling distance of 5.2 km, the error may go beyond the nominal 10 K (5 K) with a probability of 50%
 344 For 9.2 km sampling distance, and the maximum sampling error is always above the nominal values for
 345 some region and/or a day in the year. Even if we require that the nominal error is undercut only with a
 346 probability of 70% for all pixels and days, a sampling distance of 800 m is not enough. If only 50% of all
 347 networks are required to fulfill the 10K/(5K) bound, a sampling distance of 10 km is sufficient.

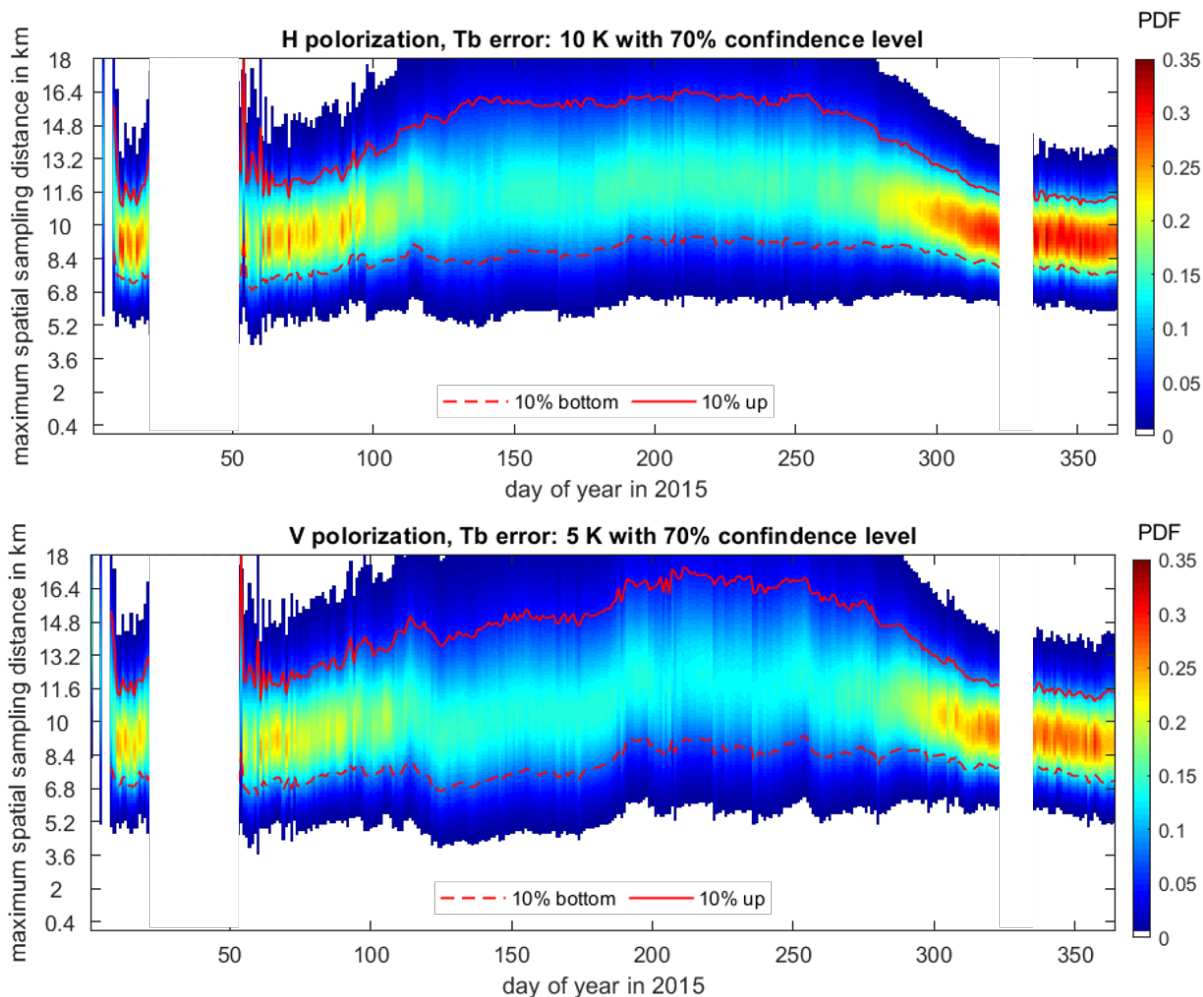


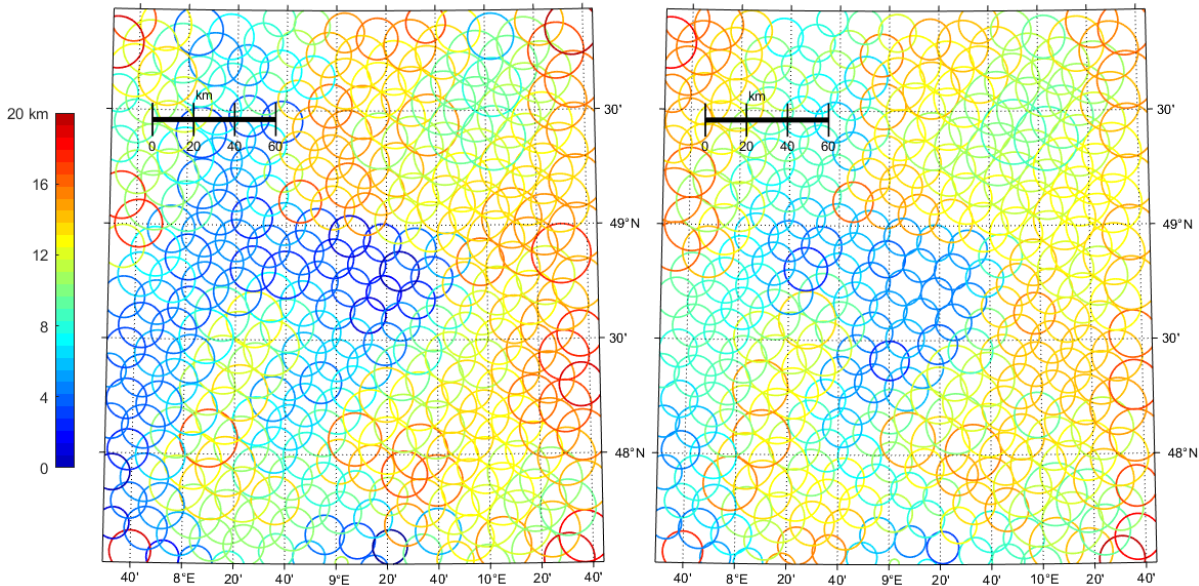
Figure 7: Time series of the distribution of maximum sampling distances (70% confidence in 10K/5K for H/V polarization) for brightness temperature at every sites in 2015. The color indicates the probability of occurrence.

348

349 The time series of the distribution of the maximum sampling distances for brightness temperature
 350 (Figure 7) is quite similar to the one for the maximum sampling distances for soil moisture. Figure 7 only
 351 illustrates the periods without freeze/thaw state transformations, and liquid water in the soil dominates
 352 the brightness temperature signal. Values range from 6.8 km to 16.4 km for most cases. The spread of the

353 sampling error has, however, a distinct seasonal variation; e.g., the maximum sampling distance for 90
354 percent of the footprints is 11.6 km from DOY 100 to 275 and 8.8 km for the rest of the year.

355 The spatial distribution of the annual maximum sampling distance allowed to guarantee a sampling
356 error less than 10K/5K for H/V polarized brightness temperatures and its RMS for the year 2015 (Figure 8)
357 are similar for H and V polarizations, but shows a substantial spatial contrast compared to the results for
358 soil moisture (Figure 5). Again, the southeast corner of the model region allows for larger maximum
359 sampling distances, but there are now also other distinct regions with larger allowed maximum
360 distances. Additional input parameters required - especially LAI - and internal parameters in CMEM
361 additionally impact the representativeness of sites for brightness temperatures. LAI dominates the
362 variation of the representativeness of ground-based observations and also its temporal variation, as can
363 be inferred from the correlation between large maximum sampling distances with its variability over the
364 year (correlation coefficient is 0.84/0.83 for H/V polarization), which is not observed for soil moisture. LAI
365 is the only input in CMEM, which can lead to such a temporal variation because other parameters such as
366 air temperature, soil moisture, soil properties, etc. are either fixed or do not impact as strongly the
367 brightness temperature.



368 Figure 8: Spatial distribution of the maximum distances of stations (diameter of circles, see scale) for
369 surface-based brightness temperature observations required to keep the sampling error below 10 K
370 for H polarization (left panel) and 5 K for V polarization (right panel). The color of the circles (see color
bar) gives the RMS of the maximum sampling distance over time for the year 2015.

369 3.3 Maximum sampling distance differences between soil moisture and brightness 370 temperature

371 The differences in the variability of the maximum allowed sampling distance for soil moisture and
372 brightness temperature can be explained by using the microwave transfer model CMEM. The relationship
373 between soil moisture and brightness temperature is complex and non-unique (Figure 9a, b). For example,
374 a soil moisture value of $0.4 \text{ cm}^3/\text{cm}^3$ relates to brightness temperatures from 180 K to 250 K for H
375 polarization and 225 K to 265 K for V polarization due to the variation of vegetation cover, soil properties,
376 and terrain.

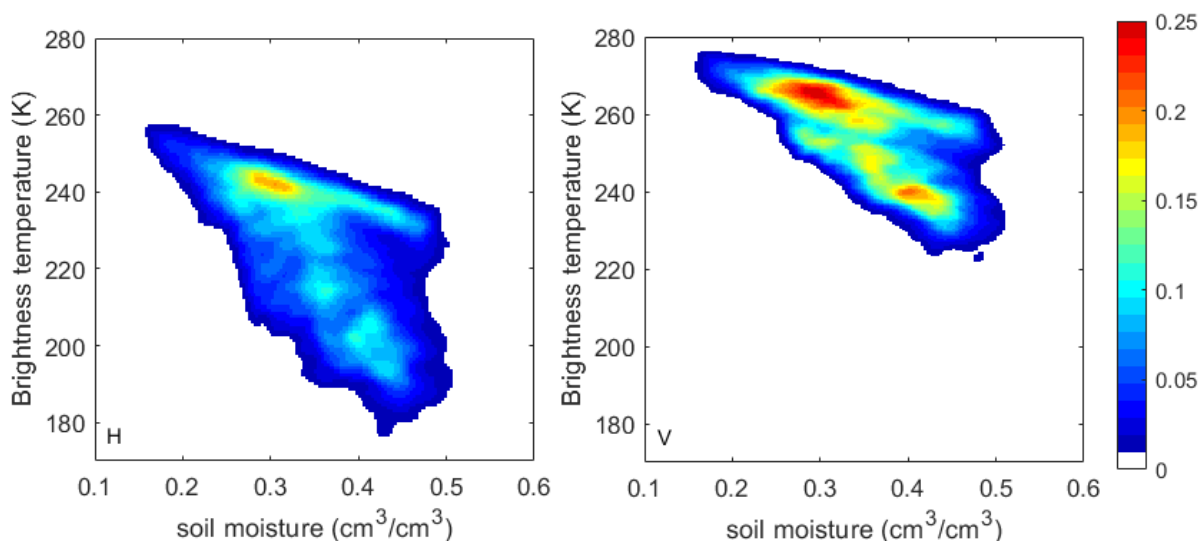


Figure 9: Scatter plots of the joint PDF between brightness temperature at H (left) and V (right) polarization against soil moisture computed from the 400 m resolution virtual reality for one year. Both the temporal and spatial variation is included.

377
378 As already mentioned in the introduction, the spatial resolution for the SMAP active product is 3
379 km and for the passive-active merged soil moisture product 9 km. SMAP CAL/VAL requires three stations
380 for the evaluation of the prior and five stations for the latter product (Colliander et al., 2017b). We
381 computed the station distance required to keep the sampling error below the nominal $0.04 \text{ cm}^3/\text{cm}^3$ for
382 both products by using the same methodology used above. Due to limited computation capacity, only the
383 higher-resolution pixels in the center of the 43-km SMOS footprints are evaluated. According to the results
384 (Figure 10), the probability that 3 km and 9 km pixels sampled with 3 and 5 stations, respectively, have
385 sampling errors below the nominal value of $0.04 \text{ cm}^3/\text{cm}^3$ is below 40% and thus much lower than the
386 required 70%. The temporal variation of the confidence level is larger for the 3 km than for the 9 km grid
387 size.

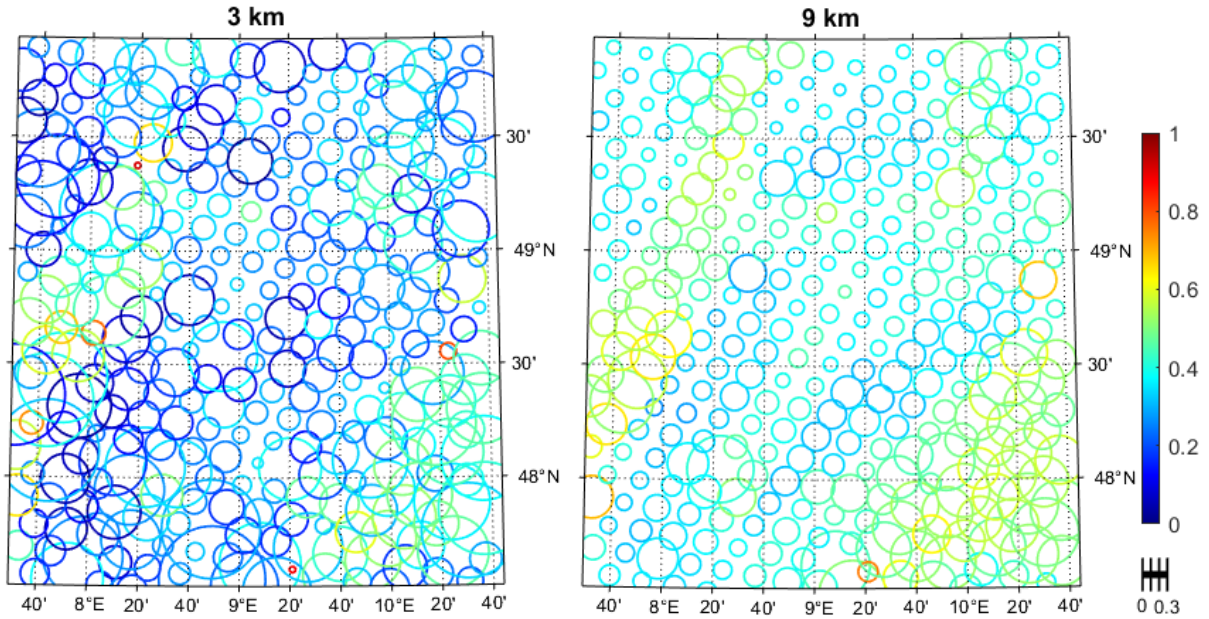


Figure 10: The spatial distribution of the soil moisture sampling confidence to achieve the 0.04 cm³/cm³ accuracy requirement by sampling 3 km (left) and 9 km footprints (right) with 3 and 5 sites, respectively (see the scale below the color bar). The colors show the minimum confidence level throughout the year 2015 for every footprint. The scale is soil moisture accuracy that can be achieved.

388

389 **3.4 The impact of land surface inhomogeneity**

390 Areas with vegetation water content above 5 kg/m² (mostly forests) are flagged in SMAP retrievals. The
 391 networks used in the studies (Colliander et al., 2017b; Famiglietti et al., 2008) were selected because of
 392 their relative homogeneity; thus, forested patches, open water, permanent ice and snow, urban areas,
 393 and wetlands are excluded. Soil moisture maps from SMAP/SMOS are, however, global. Thus estimates
 394 are provided everywhere; hence, signals from open water surfaces on sub-grid scales may influence the
 395 products. We used our simulated observations to study the impact of sub-pixel contributions of forested
 396 areas on the sampling errors.

397 In total, only 16 of the 320 footprints covering the model area have forest fractions below 15%
 398 and negligible surface water contributions; such footprints are usually considered ideal for soil moisture
 399 Cal/Val. In terms of both soil moisture and brightness temperature, their maximum sampling errors are
 400 considerably lower compared to all sites for all sampling distances (Figure 11). Thus, excluding sites with
 401 larger forest fractions leads to lower sampling errors.

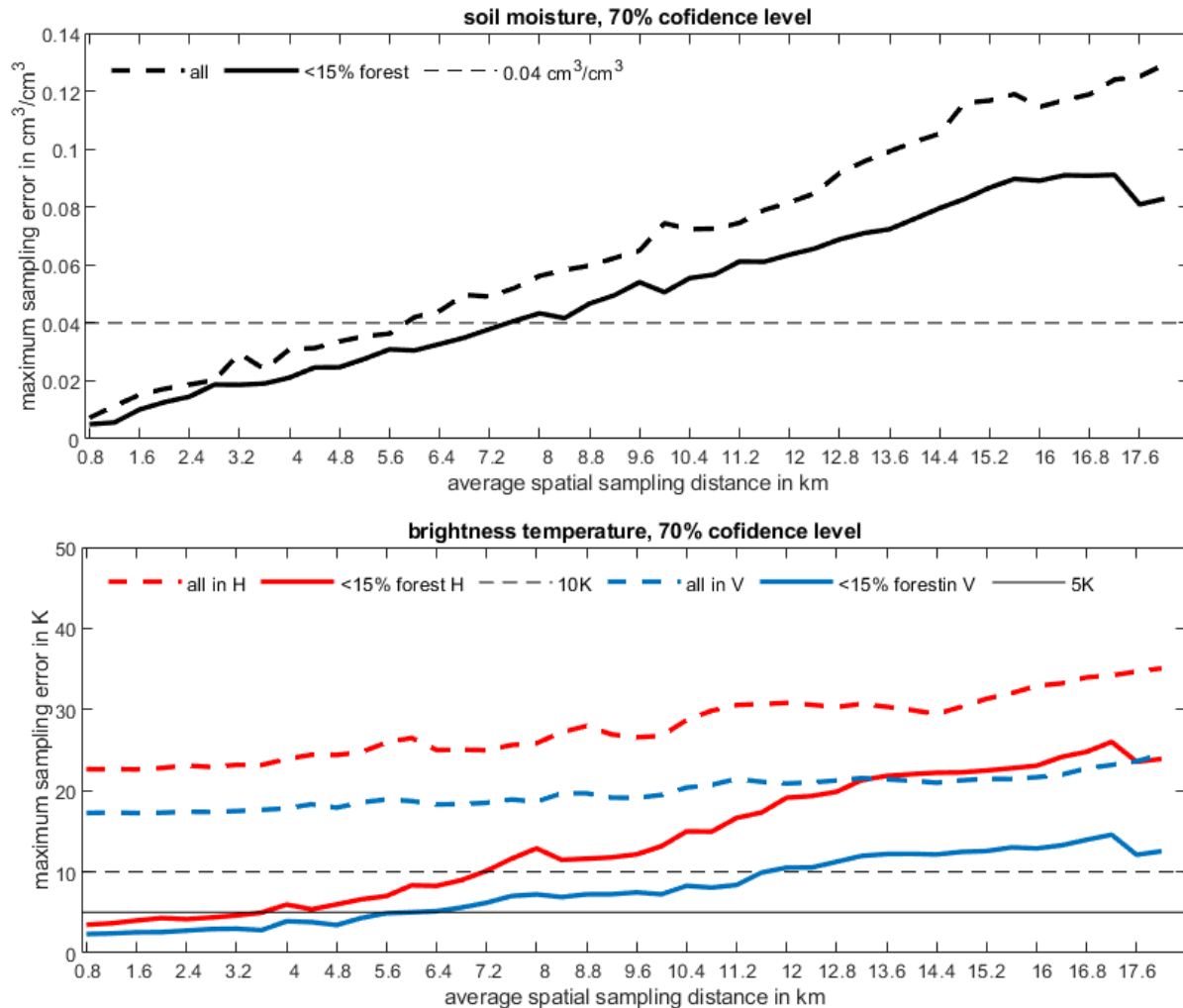


Figure 11: The maximum sampling errors of the arithmetic mean of soil moisture (top) and brightness temperature (bottom) estimated from all sites and from sites with forest cover below 15 % against average sampling distance.

402

403 The results shown in Figure 11 do not mean that forest sites always have higher soil moisture errors than
 404 non-forest sites, but by picking Cal/Val sites with favorable conditions reduces the required sampling
 405 density, which may, however, affect their representativeness. Moreover, the required sampling density
 406 inferred from non-forest sites cannot be extended to forest sites.

407 **4. Conclusion and discussion**

408 We used a virtual reality generated with a fully coupled subsurface-vegetation-atmosphere model
 409 platform over southwestern Germany with a spatial resolution of 400 m for the land components to
 410 quantify the sampling error for the arithmetic averaged soil moisture and the weighted average brightness
 411 temperatures estimated from in-situ ground-based observation networks covering SMOS/SMAP-like
 412 footprints of 43 km diameter for a wide range of potential sampling distances. By using a virtual reality

413 at such high resolution, we have a physically consistent three-dimensional evolution of the terrestrial
414 system at our disposition from which we can take virtual soil moisture observations and – via the radiative
415 transfer model CMEM and a satellite antenna function – microwave brightness temperature observations
416 from the highest resolution at 400 m to any larger resolution.

417 We adopted as an upper threshold for the sampling error of ground-based sensor networks when
418 estimating averages over SMOS/SMAP pixels the target SMOS/SMAP soil moisture retrieval accuracy of
419 $0.04 \text{ cm}^3/\text{cm}^3$. We quantified the maximum sampling distance, which still keeps the sampling error below
420 that accuracy either for all or for 70% of all SMOS/SMAP pixels in the modeling region over one year for
421 all network configurations possible. A major assumption in our study is that the estimation of soil moisture
422 for an area with a diameter of about 400 m is possible, or in other words that a single station within a 400-
423 m area is representative for its spatial average, an assumption also discussed in Famiglietti et al. (2008).
424 Compared to the region analyzed in Famiglietti et al. (2008), our study uses a much more realistic terrain
425 and excludes subjective factors in selecting suitable Cal/Val sites. Because of this, the soil moisture error
426 in our study grows much faster with increasing sampling distance. We also find that the estimation of
427 area-averaged brightness temperatures from a network of ground-based stations has a different error
428 growth with increasing sampling distance compared to soil moisture despite an initial linear growth for
429 both of them (compare Figures 3 and 6). Thus, a representative soil moisture network does not guarantee
430 a representative radiometer network for the estimation of area-averaged brightness temperature, or that
431 brightness temperatures computed for the soil moisture stations can be used for that estimate. But
432 Figures 3 and 6 also show that sampling distances below 6 km still fulfill the 70th percentage requirement
433 for keeping the sampling error below the nominal error.

434 Besides plant types, there is no clear pattern similarity between clay/sand/elevation (Figure 1) and
435 spatial sampling distance (Figure 5). Soil properties may be related to the regional climate (annual
436 precipitation, radiation flux balance, etc.). For instance, arid regions usually contain higher sand fractions,
437 but such regions are seldom the focus of soil moisture studies because of its low variation. Transition
438 zones like our model area usually encompass various soil properties, which are often correlated with
439 landuse and vegetation and thus the plant function type used in the CLM. Topography also affects the soil
440 moisture and TB distribution, but it is difficult to infer the impact of landuse and vegetation because soil
441 properties determine both the water holding capacity and the plant cover. In practice, soil moisture
442 monitoring networks avoid complex terrain. Homogenous terrain and landscape lead to an
443 overestimation of satellite soil moisture product accuracies.

444 The statistical results in our study differ from those in Famiglietti et al. (2008) because our focus is
445 on the satellite footprint scale and not the representativeness of one station within a network. For
446 example, a particular sensor may not represent the true 400 m average, but one such sensor every 400 m
447 may statistically sufficiently represent a much larger footprint. A similar concept is adapted in ensemble
448 forecasts using members, e.g., with different physics packages, none of which is expected to be the truth
449 (Lewis, 2005; Leutbecher and Palmer, 2008). The space detected by a soil moisture sensor, which is

450 measuring the dielectric constant of the soil or other media using capacitance/frequency domain
451 technology, is about a ten-centimeter sphere. Thus, the study by Famiglietti et al. (2008) assumes soil
452 moisture homogeneity on the scale of meters. We believe that the 400-m soil moisture homogenous
453 assumption does not interfere with our conclusions and that our study can be considered as a
454 complement to the study by Famiglietti et al. (2008).

455 The calibration and validation of passive satellite-based L-band soil moisture estimates are difficult
456 due to the large sub-pixel variability (Lv et al., 2019; Lv et al., 2016b). Even with a perfect microwave
457 transfer model and perfect sensors, we can hardly find an appropriate in-situ observation to compare
458 with. While soil moisture also varies in the vertical, sensors are usually mounted at a fixed depth; thus,
459 comparisons with satellite observations require the knowledge of the microwave penetration depth,
460 which is, however, unknown in general. (Lv et al., 2018) developed a model based on the soil effective
461 temperature, which sheds light on this fundamental problem. This study isolates the sampling density
462 issue from other factors and is a test of the current Cal/Val network standard without pre-knowledge of
463 the site. The SMAP team suggests 15 sites for a 36 km by 36 km grid-size (Colliander et al., 2017b), and
464 this study agrees with this configuration for typical mid-latitude European regions from the sampling error
465 perspective. For a 36 km by 36 km grid-size, the required sampling sites would range from about 36 (6 km)
466 to 4 (17 km). However, five sites for 9 km by 9 km and three sites for 3 km by 3 km will miss the 70 %
467 confidence level requirements over this area. Since SMAP's 9-km and 3-km soil moisture products are
468 from a combination of passive and active microwave signals, which have lower accuracy than the passive
469 one (Entekhabi et al., 2010), their Cal/Val campaigns shall determine sampling distances with less
470 confidence level.

471 Our virtual reality contains extensive land cover variability (Figure 1), thus it would be helpful to
472 adopt our approach for less complex regions with variabilities closer to the typical Cal/Val station
473 networks. Overall, we find that a soil moisture sampling distance roughly below 3 km is necessary to keep
474 the sampling errors always below the nominal value. The allowance for a failure probability of 30 %
475 extends this distance to 10 km. For brightness temperatures, the sampling requirements are much more
476 strict; already at 800 m sampling distance, it cannot be guaranteed that the sampling error remains below
477 the equivalent threshold of 10K/5K for H and V-polarization, respectively, even when allowing for a 30%
478 probability of failure. The error sources in retrieving soil moisture from TB data is also large in reality but
479 not concerned in this study because VR01 and the TB produced by CMEM exclude the uncertainty except
480 the sampling distance.

481 Our results are not only useful for the planning of ground-based soil moisture networks, they also
482 contribute to a better understanding of the relation between brightness temperatures observed at the
483 ground – or simulated at high resolution - and the ones observed from satellites apart from non-linearity
484 effects of radiative transfer (e.g., Drusch et al., 1999). The study allows, e.g., to quantify to what extent a
485 bias between satellites brightness temperature and forward simulation could be explained by the spatial
486 sampling (e.g., Figures 5, 8, and 11), and to understand the similarities and dissimilarities between

487 observed soil moisture and brightness temperature time-series (Figures 4 and 7). Since ground-based soil
488 moisture networks will always cover only certain parts of a satellite pixel, a bias must be expected
489 between both. Biases in satellite and ground-based estimates of soil moisture can also be caused by the
490 different representativeness of the latter for soil moisture and brightness temperatures.

491 While the allowed maximum sampling distances do not change much over the year for soil moisture
492 - except after large-scale precipitation events which allow for larger sampling distances - it's equivalent
493 for brightness temperature has a strong seasonal variation because of the blurring effect of vegetation
494 during the growing season when brightness temperatures become more homogeneous. The spatial
495 distribution of the maximum sampling distances and their local variances behave quite differently
496 between soil moisture and brightness temperature. The spatial patterns are different, and while the
497 maximum allowed sampling distance and its variance are strongly related to brightness temperature, they
498 are barely related to soil moisture; this different behavior is caused by the complexity of other factors
499 influencing microwave radiative transfer.

500 Our study strongly suggests that the sampling density of current SMOS/SMAP ground-based Cal/Val
501 networks and the resulting potential sampling error of estimated pixel-mean soil moisture and brightness
502 temperatures considered in such studies should be reviewed carefully. We expect this study will help to
503 understand the errors of satellite-derived soil moisture better.

504

505 **Acknowledgments**

506 This research was funded by the Deutsche Forschungsgemeinschaft (DFG) via FOR2131: "Data
507 Assimilation for Improved Characterization of Fluxes across Compartmental Interfaces", subproject P2.
508 Compute time has been provided by the Gauss Centre for Supercomputing ([http://www.gauss-](http://www.gauss-centre.eu/gauss-centre/EN/Home/home_node.html)
509 [centre.eu/gauss-centre/EN/Home/home_node.html](http://www.gauss-centre.eu/gauss-centre/EN/Home/home_node.html)) operated by the Juelich Supercomputing Centre
510 (http://www.fz-juelich.de/ias/jsc/EN/Home/home_node.html). We thank the members of HPSC-TerrSys
511 (http://www.hpsc-terrsys.de/hpsc-terrsys/EN/Home/home_node.html) and Klaus Goergen in particular
512 for invaluable technical support with the JUQUEEN supercomputer. Furthermore, we thank Prabhakar
513 Shresta and Mauro Sulis from the Transregional Collaborative Research Center 32 (TR32) for their
514 preliminary work and introduction to the TerrSysMP modeling platform.

515

516 **References**

517 Ashby, S. F., and Falgout, R. D.: A parallel multigrid preconditioned conjugate gradient algorithm for
518 groundwater flow simulations, *Nucl Sci Eng*, 124, 145-159, 1996.
519 Baldauf, M., Seifert, A., Förstner, J., Majewski, D., Raschendorfer, M., and Reinhardt, T.: Operational
520 convective-scale numerical weather prediction with the COSMO model: Description and sensitivities,
521 *Monthly Weather Review*, 139, 3887-3905, 2011.

522 Baroni, G., Zink, M., Kumar, R., Samaniego, L., and Attinger, S.: Effects of uncertainty in soil properties on
523 simulated hydrological states and fluxes at different spatio-temporal scales, *Hydrol. Earth Syst. Sci.*, 21,
524 2301-2320, 10.5194/hess-21-2301-2017, 2017.

525 Bhuiyan, H. A. K. M., McNairn, H., Powers, J., Friesen, M., Pacheco, A., Jackson, T. J., Cosh, M. H., Colliander,
526 A., Berg, A., Rowlandson, T., Bullock, P., and Magagi, R.: Assessing SMAP Soil Moisture Scaling and
527 Retrieval in the Carman (Canada) Study Site, *Vadose Zone J*, 17, ARTN 180132, 10.2136/vzj2018.07.0132,
528 2018.

529 Brocca, L., Melone, F., Moramarco, T., and Morbidelli, R.: Spatial-temporal variability of soil moisture and
530 its estimation across scales, *Water Resources Research*, 46, Artn W02516, 10.1029/2009wr008016, 2010.

531 Burgin, M. S., Colliander, A., Njoku, E. G., Chan, S. K., Cabot, F., Kerr, Y. H., Bindlish, R., Jackson, T. J.,
532 Entekhabi, D., and Yueh, S. H.: A Comparative Study of the SMAP Passive Soil Moisture Product With
533 Existing Satellite-Based Soil Moisture Products, *Ieee Transactions on Geoscience and Remote Sensing*, 55,
534 2959-2971, 10.1109/Tgrs.2017.2656859, 2017.

535 Chen, F., Crow, W. T., Colliander, A., Cosh, M. H., Jackson, T. J., Bindlish, R., Reichle, R. H., Chan, S. K.,
536 Bosch, D. D., Starks, P. J., Goodrich, D. C., and Seyfried, M. S.: Application of Triple Collocation in Ground-
537 Based Validation of Soil Moisture Active/Passive (SMAP) Level 2 Data Products, *Ieee Journal of Selected
538 Topics in Applied Earth Observations and Remote Sensing*, 10, 489-502, 10.1109/Jstars.2016.2569998,
539 2017.

540 Chen, F., Crow, W. T., Bindlish, R., Colliander, A., Burgin, M. S., Asanuma, J., and Aida, K.: Global-scale
541 evaluation of SMAP, SMOS and ASCAT soil moisture products using triple collocation, *Remote Sensing of
542 Environment*, 214, 1-13, 10.1016/j.rse.2018.05.008, 2018.

543 Colliander, A., Cosh, M. H., Misra, S., Jackson, T. J., Crow, W. T., Chan, S., Bindlish, R., Chae, C., Collins, C.
544 H., and Yueh, S. H.: Validation and scaling of soilmoisture in a semi-arid environment: SMAP validation
545 experiment 2015 (SMAPVEX15), *Remote Sensing of Environment*, 196, 101-112,
546 10.1016/j.rse.2017.04.022, 2017a.

547 Colliander, A., Jackson, T. J., Bindlish, R., Chan, S., Das, N., Kim, S. B., Cosh, M. H., Dunbar, R. S., Dang, L.,
548 Pashaian, L., Asanuma, J., Aida, K., Berg, A., Rowlandson, T., Bosch, D., Caldwell, T., Caylor, K., Goodrich,
549 D., al Jassar, H., Lopez-Baeza, E., Martínez-Fernández, J., González-Zamora, A., Livingston, S., McNairn, H.,
550 Pacheco, A., Moghaddam, M., Montzka, C., Notarnicola, C., Niedrist, G., Pellarin, T., Prueger, J., Pulliainen,
551 J., Rautiainen, K., Ramos, J., Seyfried, M., Starks, P., Su, Z., Zeng, Y., van der Velde, R., Thibeault, M., Dorigo,
552 W., Vreugdenhil, M., Walker, J. P., Wu, X., Monerris, A., O'Neill, P. E., Entekhabi, D., Njoku, E. G., and Yueh,
553 S.: Validation of SMAP surface soil moisture products with core validation sites, *Remote Sensing of
554 Environment*, 191, 215-231, <https://doi.org/10.1016/j.rse.2017.01.021>, 2017b.

555 Coopersmith, E. J., Cosh, M. H., Bell, J. E., Kelly, V., Hall, M., Palecki, M. A., and Temimi, M.: Deploying
556 temporary networks for upscaling of sparse network stations, *Int. J. Appl. Earth Obs. Geoinf.*, 52, 433-444,
557 10.1016/j.jag.2016.07.013, 2016.

558 Cosh, M. H., Jackson, T. J., Starks, P., Bosch, D., Collins, C. H., Seyfried, M., Prueger, J., Livingston, S., and
559 Bindlish, R.: Strategies for validating satellite soil moisture products using in situ networks: Lessons from
560 the USDA-ARS watersheds, 2017 IEEE International Geoscience and Remote Sensing Symposium (IGARSS),
561 2017, 2015-2018,

562 Crow, W. T., Berg, A. A., Cosh, M. H., Loew, A., Mohanty, B. P., Panciera, R., de Rosnay, P., Ryu, D., and
563 Walker, J. P.: UPSCALING SPARSE GROUND-BASED SOIL MOISTURE OBSERVATIONS FOR THE VALIDATION
564 OF COARSE-RESOLUTION SATELLITE SOIL MOISTURE PRODUCTS, *Reviews of Geophysics*, 50, 20,
565 10.1029/2011rg000372, 2012.

566 dall'Amico, J. T., Schlenz, F., Loew, A., and Mauser, W.: First Results of SMOS Soil Moisture Validation in
567 the Upper Danube Catchment, *Ieee Transactions on Geoscience and Remote Sensing*, 50, 1507-1516,
568 10.1109/Tgrs.2011.2171496, 2012.

569 de Rosnay, P., Calvet, J. C., Kerr, Y., Wigneron, J. P., Lemaitre, F., Escorihuela, M. J., Sabater, J. M., Saleh,
570 K., Barrie, J. L., Bouhours, G., Coret, L., Cherel, G., Dedieu, G., Durbe, R., Fntz, N. E. D., Froissard, F., Hoedjes,
571 J., Kruszewski, A., Lavenu, F., Suquia, D., and Waldteufel, P.: SMOSREX: A long term field campaign
572 experiment for soil moisture and land surface processes remote sensing, *Remote Sensing of Environment*,
573 102, 377-389, 10.1016/j.rse.2006.02.021, 2006.

574 Delwart, S., Bouzinac, C., Wursteisen, P., Berger, M., Drinkwater, M., Martin-Neira, M., and Kerr, Y. H.:
575 SMOS validation and the COSMOS campaigns, *Ieee Transactions on Geoscience and Remote Sensing*, 46,
576 695-704, 2008.

577 Dorigo, W. A., Wagner, W., Hohensinn, R., Hahn, S., Paulik, C., Xaver, A., Gruber, A., Drusch, M.,
578 Mecklenburg, S., van Oevelen, P., Robock, A., and Jackson, T.: The International Soil Moisture Network: a
579 data hosting facility for global in situ soil moisture measurements, *Hydrology and Earth System Sciences*,
580 15, 1675-1698, 10.5194/hess-15-1675-2011, 2011.

581 Drusch, M., Wood, E. F., and Simmer, C.: Up-scaling effects in passive microwave remote sensing: ESTAR
582 1.4 GHz measurements during SGP '97, *Geophysical Research Letters*, 26, 879-882, Doi
583 10.1029/1999gl900150, 1999.

584 Entekhabi, D., Njoku, E. G., O'Neill, P. E., Kellogg, K. H., Crow, W. T., Edelstein, W. N., Entin, J. K., Goodman,
585 S. D., Jackson, T. J., Johnson, J., Kimball, J., Piepmeier, J. R., Koster, R. D., Martin, N., McDonald, K. C.,
586 Moghaddam, M., Moran, S., Reichle, R., Shi, J. C., Spencer, M. W., Thurman, S. W., Tsang, L., and Van Zyl,
587 J.: The Soil Moisture Active Passive (SMAP) Mission, *P Ieee*, 98, 704-716, 10.1109/jproc.2010.2043918,
588 2010.

589 Famiglietti, J. S., Ryu, D. R., Berg, A. A., Rodell, M., and Jackson, T. J.: Field observations of soil moisture
590 variability across scales, *Water Resources Research*, 44, Artn W01423, 10.1029/2006wr005804, 2008.

591 Gasper, F., Goergen, K., Shrestha, P., Sulis, M., Rihani, J., Geimer, M., and Kollet, S.: Implementation and
592 scaling of the fully coupled Terrestrial Systems Modeling Platform (TerrSysMP v1. 0) in a massively parallel
593 supercomputing environment—a case study on JUQUEEN (IBM Blue Gene/Q), *Geosci. Model Dev.*, 7, 2531-
594 2543, 2014.

595 Jackson, T., Colliander, A., Kimball, J., Reichle, R., Crow, W., Entekhabi, D., and Neill, P.: Science data
596 calibration and validation plan, *Jet Propuls. Lab*, 2012.

597 Kerr, Y. H., Waldteufel, P., Wigneron, J. P., Delwart, S., Cabot, F., Boutin, J., Escorihuela, M. J., Font, J., Reul,
598 N., Gruhier, C., Juglea, S. E., Drinkwater, M. R., Hahne, A., Martin-Neira, M., and Mecklenburg, S.: The
599 SMOS Mission: New Tool for Monitoring Key Elements of the Global Water Cycle, *P Ieee*, 98, 666-687, Doi
600 10.1109/Jproc.2010.2043032, 2010.

601 Kerr, Y. H., Al-Yaari, A., Rodriguez-Fernandez, N., Parrens, M., Molero, B., Leroux, D., Bircher, S.,
602 Mahmoodi, A., Mialon, A., Richaume, P., Delwart, S., Al Bitar, A., Pellarin, T., Bindlish, R., Jackson, T. J.,
603 Rudiger, C., Waldteufel, P., Mecklenburg, S., and Wigneron, J. P.: Overview of SMOS performance in terms
604 of global soil moisture monitoring after six years in operation, *Remote Sensing of Environment*, 180, 40-
605 63, 10.1016/j.rse.2016.02.042, 2016.

606 Kollet, S. J., Maxwell, R. M., Woodward, C. S., Smith, S., Vanderborght, J., Vereecken, H., and Simmer, C.:
607 Proof of concept of regional scale hydrologic simulations at hydrologic resolution utilizing massively
608 parallel computer resources, *Water Resources Research*, 46, 2010.

609 Lawrence, P. J., and Chase, T. N.: Representing a new MODIS consistent land surface in the Community
610 Land Model (CLM 3.0), *Journal of Geophysical Research: Biogeosciences*, 112, 2007.

611 Lv, S., Wen, J., Zeng, Y., Tian, H., and Su, Z.: An improved two-layer algorithm for estimating effective soil
612 temperature in microwave radiometry using in situ temperature and soil moisture measurements,
613 *Remote Sensing of Environment*, 152, 356-363, <http://dx.doi.org/10.1016/j.rse.2014.07.007>, 2014.

614 Lv, S., Zeng, Y., Wen, J., and Su, Z.: A reappraisal of global soil effective temperature schemes, *Remote
615 Sensing of Environment*, 183, 144-153, <http://dx.doi.org/10.1016/j.rse.2016.05.012>, 2016a.

616 Lv, S., Zeng, Y., Wen, J., Zheng, D., and Su, Z.: Determination of the Optimal Mounting Depth for Calculating
617 Effective Soil Temperature at L-Band: Maqu Case, *Remote Sensing*, 8, 476, 2016b.

618 Lv, S., Zeng, Y., Wen, J., Zhao, H., and Su, Z.: Estimation of Penetration Depth from Soil Effective
619 Temperature in Microwave Radiometry, *Remote Sensing*, 10, 519, 2018.

620 Lv, S., Zeng, Y., Su, Z., and Wen, J.: A Closed-Form Expression of Soil Temperature Sensing Depth at L-Band,
621 *IEEE Transactions on Geoscience and Remote Sensing*, 1-9, 10.1109/TGRS.2019.2893687, 2019.

622 Molero, B., Leroux, D. J., Richaume, P., Kerr, Y. H., Merlin, O., Cosh, M. H., and Bindlish, R.: Multi-Timescale
623 Analysis of the Spatial Representativeness of In Situ Soil Moisture Data within Satellite Footprints, *Journal*
624 *of Geophysical Research-Atmospheres*, 123, 3-21, 10.1002/2017jd027478, 2018.

625 Monerris Belda, A.: Experimental estimation of soil emissivity and its application to soil moisture retrieval
626 in the SMOS mission, 2009.

627 Montzka, C., Bogaen, H. R., Weihermuller, L., Jonard, F., Bouzinac, C., Kainulainen, J., Balling, J. E., Loew,
628 A., Dall'Amico, J. T., Rouhe, E., Vanderborght, J., and Vereecken, H.: Brightness Temperature and Soil
629 Moisture Validation at Different Scales During the SMOS Validation Campaign in the Rur and Erft
630 Catchments, Germany, *IEEE Transactions on Geoscience and Remote Sensing*, 51, 1728-1743,
631 10.1109/Tgrs.2012.2206031, 2013.

632 Njoku, E. G., and Kong, J.-A.: Theory for passive microwave remote-sensing of near-surface soil-moisture,
633 *Journal of Geophysical Research*, 82, 3108-3118, 1977.

634 O'Neill, P., Chan, S., Njoku, E., Jackson, T., and Bindlish, R.: Soil Moisture Active Passive (SMAP), Algorithm
635 Theoretical Basis Document, Level 2 & 3 Soil Moisture (Passive) Data Products, Revision B, 2015.

636 Ochsner, T. E., Cosh, M. H., Cuenca, R. H., Dorigo, W. A., Draper, C. S., Hagimoto, Y., Kerr, Y. H., Larson, K.
637 M., Njoku, E. G., Small, E. E., and Zreda, M.: State of the Art in Large-Scale Soil Moisture Monitoring, *Soil*
638 *Sci Soc Am J*, 77, 1888-1919, 10.2136/sssaj2013.03.0093, 2013.

639 Oleson, K., Niu, G. Y., Yang, Z. L., Lawrence, D., Thornton, P., Lawrence, P., Stöckli, R., Dickinson, R., Bonan,
640 G., and Levis, S.: Improvements to the Community Land Model and their impact on the hydrological cycle,
641 *Journal of Geophysical Research: Biogeosciences*, 113, 2008.

642 Qin, J., Yang, K., Lu, N., Chen, Y. Y., Zhao, L., and Han, M. L.: Spatial upscaling of in-situ soil moisture
643 measurements based on MODIS-derived apparent thermal inertia, *Remote Sensing of Environment*, 138,
644 1-9, 10.1016/j.rse.2013.07.003, 2013.

645 Rosnay, P. d., Drusch, M., and Sabater, J. i. M. n.: Milestone 1 Tech Note - Part 1: SMOS Global Surface
646 Emission Model, 2009.

647 Saavedra, P. and Simmer, C., 2018. An Octave/MATLAB® Interface for Rapid Processing of SMOS L1C Full
648 Polarization Brightness Temperature. *Journal of Open Research Software*, 6(1), p.2. DOI:
649 <http://doi.org/10.5334/jors.165>

650 Sabater, J. M., De Rosnay, P., and Balsamo, G.: Sensitivity of L-band NWP forward modelling to soil
651 roughness, *International Journal of Remote Sensing*, 32, 5607-5620, 10.1080/01431161.2010.507260,
652 2011.

653 Schalge, B., Rihani, J., Baroni, G., Erdal, D., Geppert, G., Haefliger, V., Haese, B., Saavedra, P., Neuweiler,
654 I., Hendricks Franssen, H. J., Ament, F., Attinger, S., Cirpka, O. A., Kollet, S., Kunstmann, H., Vereecken, H.,
655 and Simmer, C.: High-Resolution Virtual Catchment Simulations of the Subsurface-Land Surface-
656 Atmosphere System, *Hydrol. Earth Syst. Sci. Discuss.*, 2016, 1-44, 10.5194/hess-2016-557, 2016.

657 Schalge, B., Haefliger, V., Kollet, S., and Simmer, C.: Improvement of surface run-off in the hydrological
658 model ParFlow by a scale-consistent river parameterization, *Hydrol Process*, 33, 2006-2019,
659 10.1002/hyp.13448, 2019.

660 Shrestha, P., Sulis, M., Masbou, M., Kollet, S., and Simmer, C.: A Scale-Consistent Terrestrial Systems
661 Modeling Platform Based on COSMO, CLM, and ParFlow, *Monthly Weather Review*, 142, 3466-3483,
662 10.1175/mwr-d-14-00029.1, 2014.

663 Sulis, M., Langensiepen, M., Shrestha, P., Schickling, A., Simmer, C., and Kollet, S. J.: Evaluating the
664 influence of plant-specific physiological parameterizations on the partitioning of land surface energy
665 fluxes, *Journal of hydrometeorology*, 16, 517-533, 2015.

666 Tian, Y., Dickinson, R., Zhou, L., Zeng, X., Dai, Y., Myneni, R., Knyazikhin, Y., Zhang, X., Friedl, M., and Yu,
667 H.: Comparison of seasonal and spatial variations of leaf area index and fraction of absorbed
668 photosynthetically active radiation from Moderate Resolution Imaging Spectroradiometer (MODIS) and
669 Common Land Model, *Journal of Geophysical Research: Atmospheres*, 109, 2004.

670 Ulaby, F. T., Moore, R. K., and Fung, A. K.: *Microwave Remote Sensing Active and Passive-Volume III: From*
671 *Theory to Applications*, Artech House, Inc, 1986.

672 Vereecken, H., Huisman, J. A., Bogaen, H., Vanderborght, J., Vrugt, J. A., and Hopmans, J. W.: On the value
673 of soil moisture measurements in vadose zone hydrology: A review, *Water Resources Research*, 44,
674 W00d06, 10.1029/2008wr006829, 2008.

675 Zeng, X., Shaikh, M., Dai, Y., Dickinson, R. E., and Myneni, R.: Coupling of the common land model to the
676 NCAR community climate model, *Journal of Climate*, 15, 1832-1854, 2002.

677